ON TURBULENCE AND MIXING AT THE TOP OF A GRAVITY CURRENT OVER A ROUGH SURFACE

Giulia Ravizza Garibaldi[1], Annalisa Di Bernardino[2], Giovanni Leuzzi[1], Agnese Pini[1], Giorgio Querzoli[3], Paolo Monti[1]

[1]Department of Civil, Building and Environmental Engineering, Sapienza University of Rome, Rome, Italy
[2]Department of Physics, Sapienza University of Rome, Rome, Italy
[3]Department of Civil, Environmental Engineering and Architecture, University of Cagliari, Italy

Corresponding Author: Paolo Monti, email: paolo.monti@uniroma1.it

ABSTRACT

This study investigates experimentally the effects of surface roughness on turbulence and vertical mixing at a sheared density interface forming at the top of a dense current flowing over a horizontal surface. The experiments were conducted in a water channel using the lock-exchange technique. Two cases were considered: one with a smooth channel bottom, and the other with the bottom made rough by means of a series of parallelepiped elements about one-sixth the height of the dense current. Feature Tracking and Planar Laser-Induced Fluorescence techniques were used to measure fluid velocity and density, respectively. Results show a general sensitivity of the mean flow and turbulence variables on surface characteristics. In the rough case, the density interface is thinner and some of the main parameters involved in the turbulence kinetic energy equation, e.g., buoyancy, production, and its dissipation rate, are higher than in the smooth case. Similarly, turbulent diffusivities of mass and momentum also depend on roughness, although their ratio remains practically unchanged going from the smooth to the rough surface. Finally, some of the results are consistent with field data and numerical simulations found in the literature.

1. INTRODUCTION

Kelvin-Helmholtz (KH) waves (or billows) are distinct, periodic, vortical structures that can form within a stably stratified interface in the presence of a velocity shear.[1] KH waves play a role in various engineering and geophysical contexts, including atmospheric turbulence and oceanic mixing, as density stratification affects vertical mixing of momentum, heat, and scalars, which are inhibited due to negative buoyancy force. In natural flows, variations in density can be generated by changes in temperature, as usually occurs in the atmosphere and lakes, or in salt concentration, as in seas and oceans.[2-5]

KH waves are one of the main causes of turbulence generation in stably stratified conditions. They appear when the destabilizing effect of the velocity shear prevails over the stabilizing effect of buoyancy. Miles[6] and Howard[7] demonstrated that a laminar, inviscid flow in an unbounded domain becomes turbulent when $R_g < 1/4$ somewhere within the fluid. Here, $R_g = N^2/(dU/dz)^2$ is the gradient Richardson number, $N = [-(g/\rho_0)d\rho/dz]^{1/2}$ is buoyancy frequency, U the streamwise velocity, ρ the density, ρ_0 the reference density, g the gravity acceleration, and z the vertical coordinate. Initially, the growth of sinusoidal-looking perturbations up to a finite amplitude is observed. Then the interface rolls in on itself, and a series of vortices form, finally leading to their breakup and the emergence of turbulent regions. Depending on the interaction with the initial velocity and density gradients, such turbulence may persist over time or decay rapidly.[8] The energy associated with vortices is partly dissipated, partly converted back into kinetic energy, because of the partial fluid re-stratification, and partly expended in mixing, causing a vertical transfer of density, i.e., an irreversible increase of flow potential energy.[9] This process has broad implications for natural flows: in the atmosphere, KH billows contribute to cloud formation and drive turbulence in jet streams, while in oceans they influence nutrient transport and heat exchange along the water column. By improving our understanding of turbulence in stably stratified flows, it is possible to refine predictive numerical models, with applications ranging from climate modeling to engineering flows.[10,11]

KH waves study has been approached through various theoretical, experimental, and numerical methods. Given their transient nature, analysis of KH waves based on field observations is rather difficult.[12] Analytical models based on linear stability analysis provide insight into the onset of the instability[6], while laboratory experiments and numerical simulations help elucidate the nonlinear evolution and the three-dimensional structure of KH billows.[9,13-16] Recent advancements in computational fluid dynamics have allowed for high-resolution numerical simulations that capture fine-scale turbulence and mixing properties associated with billow breakdown.[17,18]

Despite significant progress, parameterization of the turbulence variables of interest for stably stratified flows remains an open research field, e.g., downslope winds over mountain ridges[19-22], density currents above urban canopies[12], or over arrays of regular obstacles.[23] The latter authors analyzed the dynamics

of the density current front in detail, paying attention also to the potential energy of the flow and the entrainment at the interface. To gain deeper insight into this field of research, this paper focuses on the role played by surface characteristics on turbulence and mixing within the sheared density interface forming at the top of a dense current flowing over a horizontal surface. Two different experimental conditions were analyzed: the first with a smooth and the second with a rough bottom. The collected data made it possible to determine eddy diffusivities of momentum and mass, as well as other parameters of interest in turbulent flow modelling.

The outline of the paper is as follows. The experimental setup and data analysis are described in section 2, while the results are shown and discussed in section 3. Final remarks and conclusions are given in section 4.

2. EXPERIMENTAL SETUP AND DATA ANALYSIS

The experiments were carried out in a water channel 7.40 m long (x-axis), 0.25 m wide (y-axis) and with a working depth of 0.35 m (z-axis), as sketched in Figure 1a. The technique used is lock exchange, which has been widely adopted in other valuable laboratory studies concerning gravity-driven flows and KH wave breaking.[22-28] The channel is subdivided into two separate sections by a movable gate. The left side of the channel (length $x_0 = 2.90$ m) is filled with a mixture of salt and fresh water having a density higher than that of the fresh water filling the right section. A fluorescent dye (Rhodamine-WT) is added to the saline solution in order to apply Planar Laser-Induced Fluorescence (PLIF) technique for fluid density measurements.[29] The density difference between the two sections is $\Delta\rho$ = 6.90 kg m^{-3}, which corresponds to a reduced gravity $g' = g\Delta\rho/\rho_0 = 0.067\ \mathrm{ms}^{-2}$, a buoyancy velocity: $U_0 = \sqrt{g'H_0} = 0.13\ \mathrm{ms}^{-1}$, a bulk Richardson number $R_0 = g'H_0/2\,(U_0)^2 \sim 0.50$, a bulk buoyancy frequency $N_0 = \sqrt{g'/H_0} \sim 0.50\ \mathrm{s}^{-1}$, and a bulk Reynolds number $Re_0 = U_0H_0/\nu \sim 32000$, where $H_0 = 0.25$ m is water depth, ν water kinematic viscosity, and ρ_0 average density. The salt concentration is small enough not to produce a significant optical disturbance during image acquisition.

The acquisition facility consists of a green laser (5 W, wavelength 532 nm) that illuminates a vertical section nearly 2-mm thick passing through the longitudinal axis of the channel, and of two synchronized cameras (1024x1280 pixel resolution), which grab 100 images per second on an investigated area 73.0 mm tall (z-axis) and 91.0 mm long (streamwise). The two cameras are aligned horizontally to optimize framing of the area of interest and to reduce image distortion as much as possible. Flow velocity and dye concentration are measured simultaneously on the acquisition plane by means of Feature Tracking[30] (FT) and PLIF techniques, respectively. The first camera captures the positions of non-buoyant particles (pine pollen particles, ~20 μm in diameter) premixed in both fluids and allows for the assessment of instantaneous velocity fields by image analysis-based FT. The sparse, instantaneous velocity samples yielded by FT were interpolated on a regular grid by a Gaussian-weighted function. The optimal step

width (10 pixel, i.e. ~0.7 mm) was chosen based on sensitivity and convergence tests. As a result, instantaneous velocity fields at 100 Hz on a regular 102x128 array are obtained.

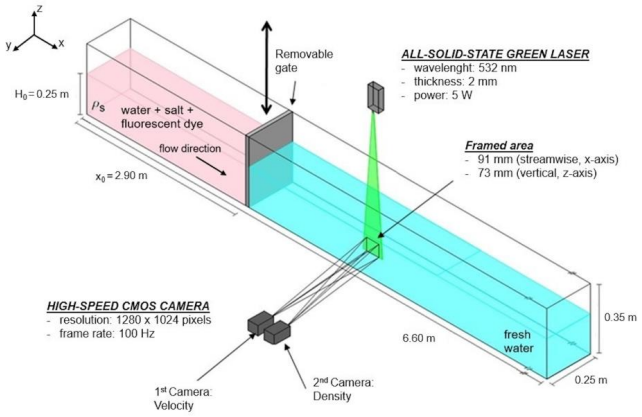

(a)

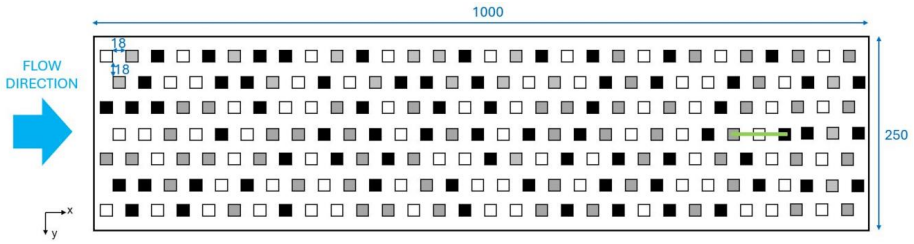

(b)

FIG. 1. (a) A sketch of the experimental apparatus. (b) Schematic top view of the roughness element array. The white, the black, and the grey parallelepipeds are 20 mm, 17.5 mm, and 15 mm tall, respectively (their base area is 15x15 mm^2). The green line is the signature of the vertical interrogation area. Measurements are in mm.

The second camera captures the light fluoresced by the Rhodamine-WT, the latter being a non-reactive dye that, when excited at 532 nm, emits at 587 nm. Only fluorescence is captured by the camera thanks to a narrow band-pass filter tuned to 587 nm. Fluid density is determined in each pixel of the frame relating density to the measured pixel brightness – the latter depending on the fractional volume of the dyed fluid–, which, in turn, is proportional to salt concentration. The relationship between brightness and dye concentration was established by a careful calibration procedure. The density field is mapped onto the velocity field by means of an affine transformation that minimizes the unavoidable distortions due to the different viewpoints of the two cameras. The spatial resolution of the density field is pixel

size, i.e., ~0.07 mm.

The acquisition frequency of the two cameras was chosen based on the time scales relevant to the smallest eddies of the turbulence field, namely Kolmogorov's, $T_K = (\nu/\varepsilon)^{1/2}$, and Batchelor's, $T_B = (D / \varepsilon)^{1/2}$, time scales. Here, ε is dissipation rate of turbulence kinetic energy (t.k.e.) and D molecular diffusivity of Rhodamine-WT. T_K and T_B represent the time scale of the dissipating eddies and that of the finer structures of the concentration field, respectively. For the present experiment $D \sim 10^{-9}$ $m^2 s^{-1}$ and $\varepsilon \sim 10^{-4}$ $m^2 s^{-3}$, the latter to be considered as representative of the interfacial layer (see below). Hence, $T_K \sim 0.1$ s and $T_B \lesssim 0.005$ s. This ensures that the sampling interval (0.01 s) is small enough to allow proper analysis of the smallest eddies but may not be entirely adequate for estimating the finer structures of the concentration field.

Surface roughness was modelled by means of an array of parallelepipeds with a base area of 15x15 mm^2 glued onto the channel bottom of the right volume in an aligned pattern with planar area index $\lambda_P = A_P/A_T = 0.2$ (Fig. 1b), where A_P is plan area of the obstacles and A_T is array area. The height of the parallelepipeds varies between 15.0 mm and 20.0 mm (average height h = 17.5 mm). The chosen λ_P corresponds to the wake-interference regime ($0.13 < \lambda_P < 0.35$), in which obstacles are close enough that the wakes strengthen each other.[31,32] The frontal area index, i.e., the total parallelepiped vertical area facing the flow direction per unit bottom area is λ_F=0.22, while the standard deviation of parallelepiped height is 2.04 mm, i.e., 14% of h.

The experiment starts by releasing the lock, which allows the denser fluid to slump left to right underneath the lighter fluid, forming a gravity current nearly 100 mm deep lasting about 120 s. This has a sharp density front at its leading edge, while a stable density stratification forms behind the front. A backward flow moves leftward above the dense current. After the passage of the front, a quasi-stationary regime lasting nearly 35 s is established, during which the current depth does not change appreciably. Figure 2 shows an example of density time histories acquired along a vertical profile passing through the channel axis 1.00 m downwind of the gate for the rough, Fig. 2a, and the smooth, Fig. 2b, cases (density increases from purple, fresh water, to red, mixture of salt and fresh water).

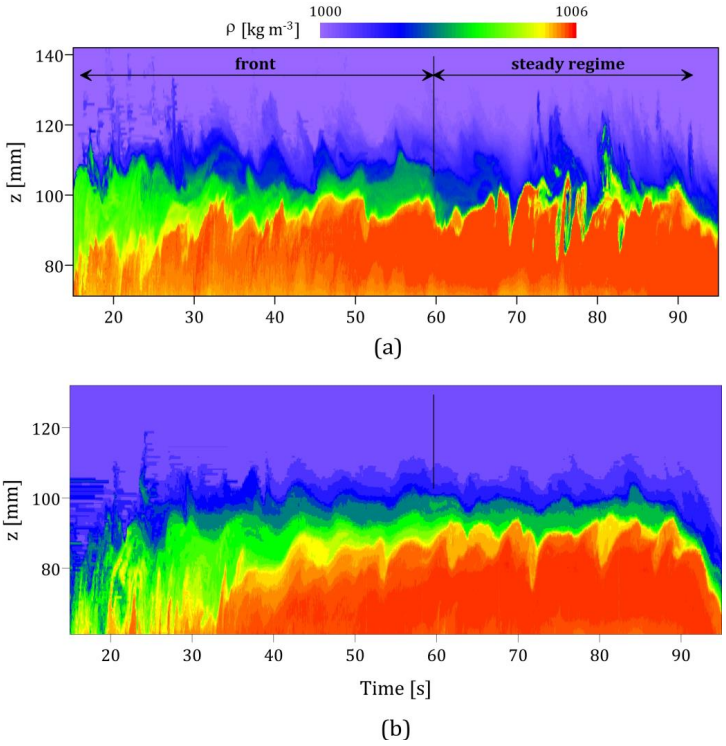

FIG. 2. Example of density time history acquired along a vertical profile passing through the center of the framed area for (a) rough bottom case and (b) smooth case. The channel bottom (z=0) is not included in the picture.

During the quasi-steady regime, mean streamwise, $\bar{u}$, and vertical, $\bar{w}$, velocity components, standard deviations, $\sigma_u = \sqrt{\overline{u'^2}}$ and $\sigma_w = \sqrt{\overline{w'^2}}$, vertical turbulent momentum flux, $\overline{u'w'}$, mean density, $\bar{\rho}$, and vertical turbulent density flux, $\overline{w'\rho'}$, are determined on the 102x128 array by applying canonical Reynolds averaging procedure (bar indicates mean value and prime fluctuation around the mean). Note that the chosen averaging interval, 35 s (i.e., 3500 frames), is about $16T_0$ ($T_0 = 1/N_0$ is buoyancy time scale), which can be considered long enough to ensure that the statistics are reasonably robust. Experiments for each of the two cases were performed four times to verify their repeatability. The errors, estimated for each variable as the average over all data points, are a few percent for the streamwise velocity and density, while 10–25% for the higher-order statistical moments.

Before the analysis of the results, a discussion on the weaknesses of our measurement setup is necessary. First of all, the assumed two-dimensionality of the flow field. Needless to say that the flow is three-dimensional, so some of its salient features cannot be analyzed. For example, t.k.e. dissipation rate cannot be evaluated except by the use of approximate formulas, which are sometimes hardly applicable

to the case examined in this work, though we measure on a symmetry plane. Furthermore, light absorption along the water column could worsen the quality of density measurements.[33] However, this effect is not very significant in the interface region, as the optical path of the laser light through highly dyed fluid is modest there. Finally, to avoid unwanted effects due to the attenuation of the laser light along the x-direction, the data analysis refers to the most central part of the interrogation area.

3. RESULTS AND DISCUSSION

3.1. Mean flow and turbulence characteristics at the density interface

A first difference between the two cases analyzed can be appreciated by visually inspecting the time histories of density after the steady state has been established (Figure 2). In fact, in the rough case, the wave motion at the density interface is clearly more pronounced and shows the typical structures of regimes characterized by Kelvin-Helmholtz billowing. In the smooth case, on the other hand, the interface is less irregular, although it retains a typically wave-like character. As shown below, this difference is accompanied by notable changes in the turbulent characteristics of the two flows.

In the following plots, the vertical distance from the channel bottom is normalized with the average height of the roughness elements, i.e., $z^* = z/h$. The variables of interest will be presented and discussed by considering their vertical profiles – spanning the height range of $4.5<z^*<7.5$ – passing through the center of the interrogation area (z = 0 refers to channel bottom). For ease of comparison, all the profiles corresponding to the smooth bottom (hereinafter SC, blue crosses) were shifted ~10.0 mm upward to match the height at which the mean streamwise velocity for the rough bottom (RC, red diamonds) becomes zero ($z^* \sim 5.90$, hereinafter $z^*_{\bar{u}=0}$). The different heights at which the streamwise velocities are zero in the two cases are partially due to current lifting produced by the roughness elements. Note that RC and SC share the same bulk Richardson and Reynolds numbers.

The vertical profiles of the mean streamwise velocity and density are shown in Figs. 3a and 3b, respectively. The dense current flows to the right ($\bar{u} > 0$), while the backward current to the left ($\bar{u} < 0$, Fig. 3f). A notable difference between the two cases is the thinner density interface for RC, δ_{RC}, compared to SC, δ_{SC}. These were identified as equal to the difference in height between the density jumps across the interface. While δ_{SC} is quasi-symmetrical with respect to $z^*_{\bar{u}=0}$, δ_{RC} is not, as it is significantly thinner in the dense flow below $z^*_{\bar{u}=0}$. The buoyancy frequency trends depicted in Fig. 3c reflect this occurrence. This also affects the height of the maximum velocity shear (Fig. 3d), which is located below $z^*_{\bar{u}=0}$ for both SC and RC. Careful inspection of the flow reveals that KH waves develop and collapse mainly below $z^*_{\bar{u}=0}$. A consequence of this is that also turbulence production, buoyancy, and σ_w peak below $z^*_{\bar{u}=0}$ (Fig. 4). The smaller δ_{RC} can be explained in terms of increased turbulent activity in the dense current due to larger drag exerted by the roughness elements at the channel bottom.[34] Note that this agrees with what Negretti et al.[35] found in their water channel experiments concerning analysis

of the effect of bottom roughness in two-layer flows downslope, although, in their case, this difference was greater.

Above $z^*_{\bar{u}=0}$, the mean density profile does not change appreciably going from SC to RC. On the other hand, no substantial differences between the mean streamwise velocities for the two cases are observed (Fig. 3a and 3d) apart from some deviations present in the upper portion of the backward current. This is in contrast to Negretti et al.'s results, which showed larger velocity gradients for their smooth case. The reason for this disagreement is unclear, but it might be attributed to the different nature of the roughness elements adopted in the two experiments, that is, parallelepipeds in our case instead of artificial turf, with a dense, close spacing of fine, short roughness elements as used by Negretti[35]. This is undoubtedly a crucial aspect in these fields of study, as it is reasonable to expect substantial differences in the characteristics of turbulence as the nature of the surface varies.[36]

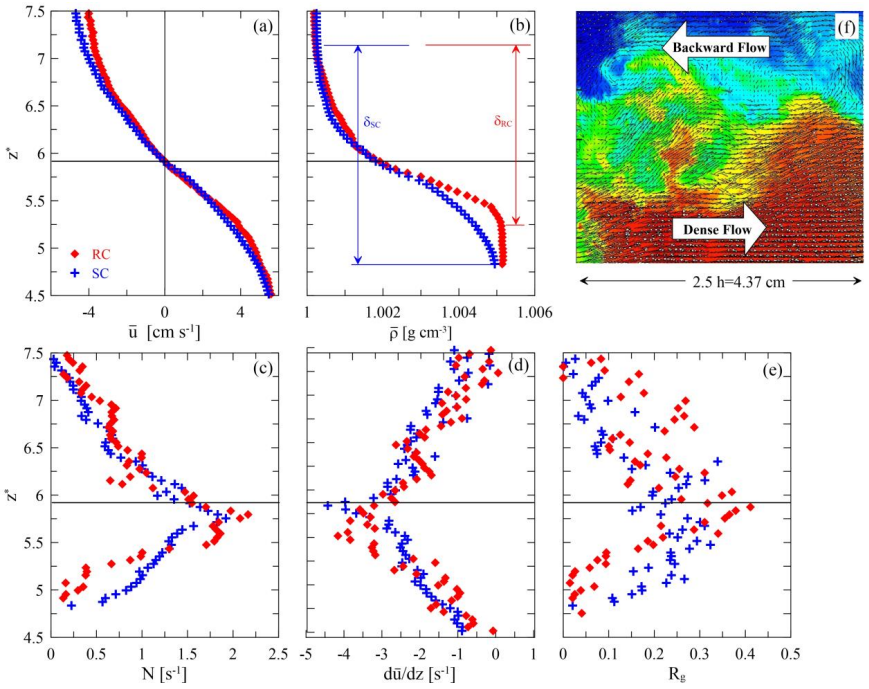

FIG. 3. Vertical profiles of (a) mean streamwise velocity component, (b) mean density, (c) mean buoyancy frequency, (d) mean velocity shear, and (e) mean gradient Richardson number. Blue crosses and red diamonds refer to SC and RC, respectively. Panel (f) shows a snapshot of density and velocity fields acquired during the breaking of a KH billow for RC (density increases from blue to red).

The differences between density and velocity gradients observed for the two cases are also reflected in the gradient Richardson number profiles (Fig. 3e) as they differ mainly for $z^* < 5.5$, where SC shows

larger R_g. Unfortunately, significant data scattering for $z^* > 5.5$ prevents us from drawing any definite conclusions for the backward current.

Other significant differences between SC and RC can be gained by looking at the turbulence variables shown in Figs. 4a-e. Overall, they are considerably higher in the rough case for $z^* < z^*_{\bar{u}=0}$ as the roughness bottom increases turbulence intensity. These values are significantly lower in the backward current (except for σ_w/U_0), where the differences between RC and SC are minimal. In that region, in fact, turbulence is patchy and generated mainly by sporadic shear instabilities, causing the turbulence to be intermittent in space and time regardless of the characteristics of the surface.

Buoyancy, B, and t.k.e. production, P, terms,

$$B = \frac{g}{\rho_0}\overline{w'\rho'} \quad , \quad P = -\overline{u'w'}\frac{d\bar{u}}{dz} \tag{1}$$

of t.k.e. equation are also higher for RC in the dense current (Figs. 4c and d), mainly due to larger vertical turbulent momentum and mass fluxes (not shown).

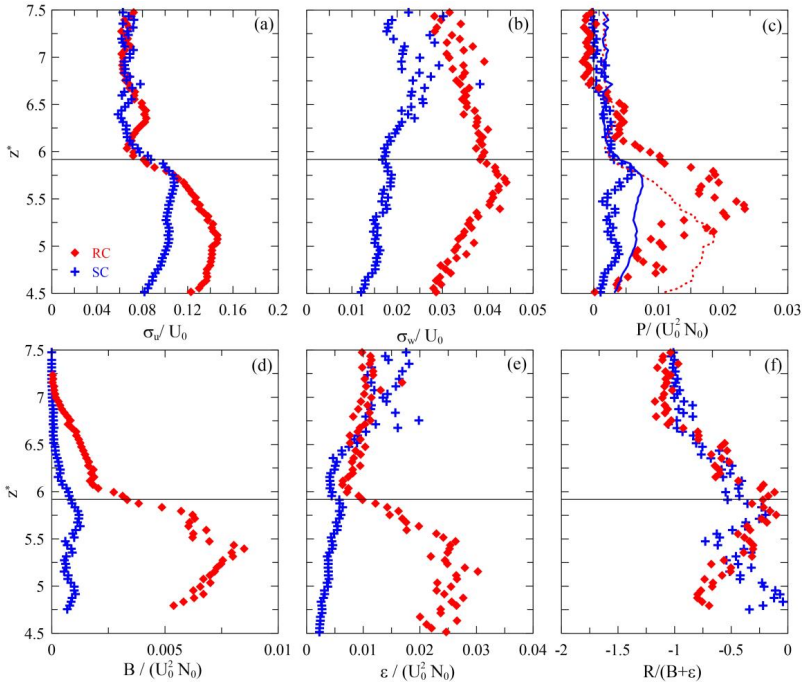

FIG. 4. Vertical profiles of normalized (a) standard deviation of the streamwise velocity component, (b) standard deviation of the vertical velocity component, (c) production term, (d) buoyancy term, (e) dissipation rate of t.k.e., and (f) residual term (Eq. 4). Continuous blue and dotted red lines in (c) have been obtained using Taylor's formula (see text). Note the different normalization adopted for R in panel f.

Both P and B profiles shown in the figure are made non-dimensional by $U_0^2 N_0$. Figure 4c displays comparisons of P with u'^3/ℓ (Taylor[37], sometimes considered as a proxy for P), where ℓ represents a suitable linear dimension of the turbulent field – in the present case, assumed equal to the thickness of the interfacial layer. The agreement between the two trends is reasonable, although for RC P peaks at a higher z^*, i.e., where σ_u/U_0 attains its maximum. It is worth noting that, unlike the other variables shown here, P does not change much going from SC to RC for $z^* < 5.25$. Since the vertical momentum flux ($\overline{u'w'}$, not shown) for RC is larger compared to SC in that region, that is due to the smaller velocity gradients observed for the rough case.

Figure 4e shows the vertical profiles of the normalized dissipation rate of t.k.e., ε, estimated using[38]:

$$\varepsilon = \frac{15}{4}\nu\left[\overline{\left(\frac{\partial u'}{\partial z}\right)^2 + \left(\frac{\partial w'}{\partial z}\right)^2}\right] \tag{2}$$

Equation 2 is particularly suitable for the present dataset as it involves only the two components of the fluctuating part of the strain rate tensor available through the field of the measured velocity vector. It is worth noting that Eq. 2 is one of several expressions of ε reported in the literature, all of which are based on simplifying assumptions about the nature of the flow. Therefore, all of them should be considered as approximations of ε. In consonance with the quantities shown earlier, ε is larger for $z^* < z^*_{\bar{u}=0}$ and its order of magnitude is consistent with that found in a similar experiment by Maggi[22] by assuming Kolmogorov's similarity hypothesis ($\varepsilon = P$). It should be noted that our ε profile is scattered in the highest region of the backward current for SC, and the large values obtained there must be taken with a certain degree of caution.

3.2. Turbulence kinetic energy budget

P, B, and ε appear in the t.k.e. equation, which under the hypothesis of parallel flow along the x (streamwise) direction reads:

$$\frac{\partial q}{\partial t} + \bar{u}\frac{\partial q}{\partial x} = P - B - \varepsilon - TT \tag{3}$$

where $q = \overline{u_k'^2}/2$ is t.k.e. (u'_k are the three components of the velocity fluctuation), while $TT = \partial/\partial x_j\left(\overline{u_k'^2 u'_j}/2 + \overline{p' u'_j}/\rho\right)$ is the spatial transport of q.[39] Equation 3 can be rearranged as:

$$R = P - B - \varepsilon = \frac{\partial q}{\partial t} + \bar{u}\frac{\partial q}{\partial x} + TT \tag{4}$$

where R assumes the meaning of a residual term, which is equal to zero only under the assumption of stationarity, horizontal homogeneity, and in the absence of diffusive flux divergence. For this case, shear production balances buoyancy and dissipation rate, a condition also known as Osborn's model.[40] RC and

SC cases show very similar trends (Fig. 4f). The balance occurs mainly around $z^*_{\bar{u}=0}$, while a R attains -1 for $z^* > 6.5$ as P is nearly zero there. Note that R has been normalized with (B+ε), i.e., the subtractive term of the t.k.e. equation, in order to better emphasize the weight of R compared to the other contributions. Since our measurement system cannot determine TT and q, we can only speculate that contributions to R could be mainly associated with t.k.e. horizontal transport in the regions of higher streamwise velocity.

3.3. Turbulent Diffusivities

Assessment of turbulent diffusivities is of great interest in engineering practice and natural flows studies since their knowledge is essential in Computational Fluid Dynamics (CFD) models used for turbulent flows and pollutant dispersion modelling in both atmospheric and aquatic systems. They are commonly determined experimentally via first-order closure as the ratio of turbulent flux to the gradient of the associated mean variable. Turbulent diffusivities of momentum and mass read, respectively:

$$K_M = -\frac{\overline{u'w'}}{\frac{d\bar{u}}{dz}} \quad ; \quad K_\rho = -\frac{\overline{w'\rho'}}{\frac{d\bar{\rho}}{dz}} \tag{5}$$

Their ratio is usually expressed as $K_\rho/K_M = {Sc_t}^{-1}$, where Sc_t denotes turbulent Schmidt number. The choice of Sc_t in CFD models is not straightforward, as it is a property of the flow and not of the fluid. This makes Sc_t parameterization often challenging[41-44], as the chosen value greatly influences the quality of the results.[45]

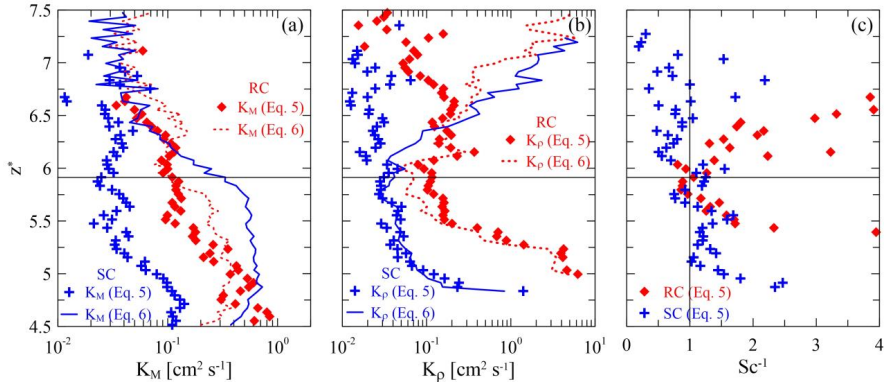

FIG. 5. Vertical profiles of (a) K_M, (b) K_ρ, and (c) inverse of the turbulent Schmidt number, ${Sc_t}^{-1} = K_\rho/K_M$, for the rough (red lines and diamonds) and the smooth (blue) cases.

Figures 5a and 5b show K_M and K_ρ determined for both the investigated cases (symbols). Two main features can be observed: firstly, K_M and K_ρ are larger for RC, and secondly, they both decrease with height and reach their minimum near $z^*_{\bar{u}=0}$. The large, unrealistic, K_ρ in the lower region of the profiles correspond with the lower edge of the density interface, where the small density gradients prevent the applicability of first-order closure. This is particularly evident for RC, which shows a thinner density interface (see Fig. 3c). This obviously affects the ${Sc_t}^{-1}$ trends (Fig. 5c), especially for RC, which shows values close to one around $z^*_{\bar{u}=0}$, while diverging away from it. The figures also show the vertical profiles of two of the most used expressions of K_M and K_ρ employed in numerical models, viz.:

$$K_M = 0.09\frac{q^2}{\varepsilon} \quad ; \quad K_\rho = \Gamma\frac{\varepsilon}{N^2} \tag{6}$$

where $\Gamma = \left(\frac{R_f}{1-R_f}\right)$ is the mixing coefficient, $R_f = B/(B+\varepsilon)$ is the flux Richardson number, and $\frac{\varepsilon}{\nu N^2}$ is the buoyancy Reynolds number, i.e., a measure of turbulence intensity in stratified shear flows. The expression for K_ρ in Eq. (6), where it is customary to assume $\Gamma = 0.2$[46], comes from the t.k.e. equation written under the assumption of R=0. The standard deviation of the spanwise velocity component (not known from our experiments) included in q has been set equal to $0.8\sigma_u^2$ based on similarity theory.[47] Despite the problems mentioned earlier, Eq. (6) reproduces K_ρ obtained by Eq. (5) for RC rather well within the dense current and part of the backward flow (up to $z^*\sim6.5$). Above it, the two formulations diverge mainly due to $N \to 0$. Another possible reason could be the high ε values for $z^* > 6.5$ (see end of section 3.1), which make K_ρ large and oscillating in the upper part of the backward current.

Similar considerations hold for SC, although the split between the two formulations occurs at lower z^*. A reasonable agreement between Eqs. 5 and 6 is also found for K_M within the whole interface for RC. In contrast, the agreement is very poor for the smooth case.

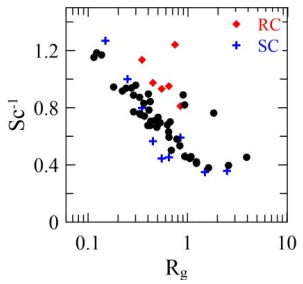

FIG. 6. Bin-averaged inverse turbulent Schmidt number as a function of the bin-averaged gradient Richardson number. Black solid circles refer to field data by Charrondier[48].

The larger Sc_t^{-1} found for RC compared to SC is reflected in the different R_g shown in Fig. 6, where the bin-averaged Sc_t^{-1} as a function of the bin-averaged R_g are depicted. As expected, Sc_t^{-1} decreases with R_g for both the cases in satisfactory agreement with field (e.g., [48,49]) and laboratory[50] data. Stable stratification damps K_ρ and this becomes increasingly important as R_g increases, since internal waves transport momentum but sustain only little (or in the ideal case of linear waves, no) buoyancy fluxes. KH billowing subsides beyond $R_g = 1$ and the dominant mixing mechanism becomes the sporadic breaking of internal waves.[50] The buoyancy flux associated with such mechanism is weaker and hence lower Sc_t^{-1} is expected. Not surprisingly, the agreement with field experiments is better for SC since the data are less affected by the small density gradient observed for RC.

3.4. Efficiency of mixing

One last aspect of interest is the dependence of the flux Richardson number, $R_f = B/(B + \varepsilon)$, also known as mixing efficiency, on the surface characteristics. As is known, R_f gives a measure of the amount of t.k.e. irreversibly converted into background potential energy. Before discussing the results, it is imperative to underline that the above expression of R_f is not free from inaccuracies as determining mixing efficiency requires calculating the diapycnal flux [9,51], which is not possible with the experimental approach used in this work. The flux Richardson number expression used here was proposed by Ivey and Imberger[52] and it does not properly account for countergradient fluxes that are expected to be important in the presence of KH billowing. However, we believe it is still worth discussing R_f trends, if only to identify possible differences associated with the bottom characteristics. The reader may refer to Venayagamoorthy and Koseff [17] for an in-depth discussion of the various definitions of R_f.

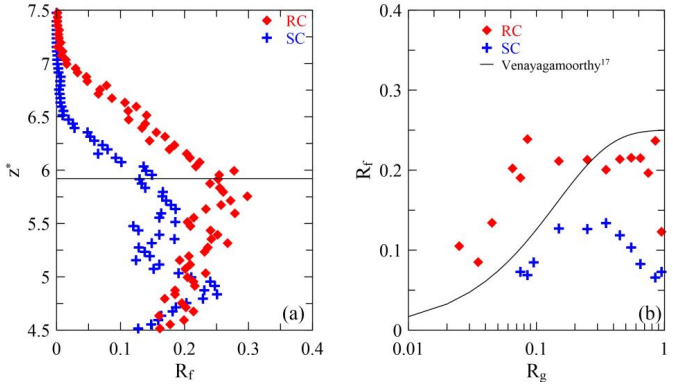

FIG. 7. (a) Vertical profiles of the flux Richardson number and (b) bin-averaged flux Richardson number as a function of the bin-averaged gradient Richardson number. The continuous line in (b) refers to the R_f formulation proposed by Venayagamoorthy[17].

We observe higher R_f for RC, close to the canonical limit 0.25 (Fig. 7a) because of the larger buoyancy flux that characterizes the rough bottom case (Fig. 4d). In other words, the larger turbulence intensity in the dense current enhances vertical mixing, and such difference is even more evident looking at the trends of the bin-averaged R_f as a function of bin-averaged R_g (Fig. 7b). The continuous line results from an analytical expression of R_f proposed by Venayagamoorthy and Koseff[17] based on Direct Numerical Simulation (DNS) data by Shih.[53] Incidentally, it is worth emphasising that the agreement between the latter and RC is reasonable, while SC always shows lower R_f values.

The difference in R_f trends between RC and SC is apparent also by analysing the mixing coefficient $\Gamma = R_f/(1 + R_f)$ versus the buoyancy Reynolds number, $\varepsilon/\nu N^2$ (Fig. 8a). The shaded areas in the figure refer to the regions enclosing some literature data, including those obtained in the laboratory by Barry[44] and by DNS by Shih[53] reported in Fig. 20.3 of Ivey[54]. The agreement with the above-mentioned works is better for RC, although the short range of the buoyancy Reynolds number of our experiments prevents us from drawing definite conclusions.

3.5. Other comparisons with field data

Comparisons with field experiments are shown in Fig. 8b, where the mixing coefficient B/ε versus the Froude number, $Fr = \varepsilon/N\sigma^2$, for the two cases are shown (σ^2 denotes velocity variance). B/ε is often used as an alternative to the flux Richardson number to model turbulent diffusivities. Dependence of B/ε on Fr has recently been proposed by Conry[55] and tested using katabatic wind data collected during the MATERHORNE field program.[56]

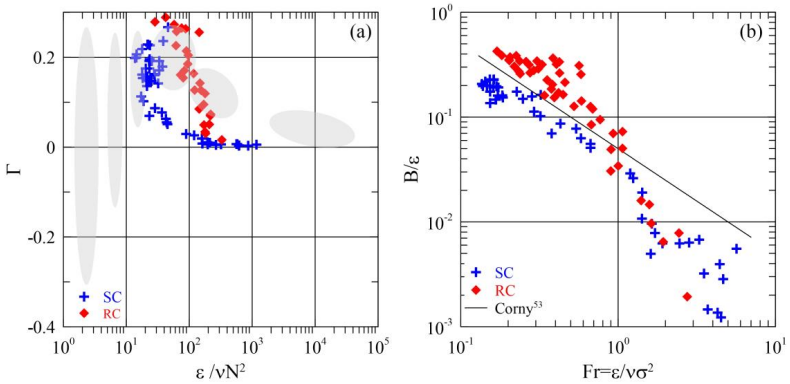

FIG. 8. (a) Mixing coefficient $\Gamma = R_f/(1 - R_f)$ as a function of $\varepsilon/\nu N^2$ (shaded areas refer to data determined from Fig. 20.3 of Ivey[54], which are based on results of Barry[46] and Shih[53]), and (b) B/ε versus Froude number Fr. Continuous line depicts the curve fit $B/\varepsilon = 0.05\ Fr^{-1}$ by Conry.[55]

In particular, based on dimensional arguments, those authors showed that B/ε depends on several non-dimensional groups, making its parameterization in environmental flows rather challenging. However,

they argued that, in equilibrium conditions, B/ε can be assumed as a function of the sole Froude number when $R_g < 0.4$, which is a condition verified for our data set. They also found that $B/\varepsilon = 0.05\ Fr^{-1}$ fits reasonably their field data points. Our B/ε for RC and SC agree reasonably with $0.05\ Fr^{-1}$ especially in the range 0.3<Fr<1, which corresponds to data points lying within the density interface. It may be of some interest to note that the points relating to Fr>1, all characterized by unsatisfactory agreement, refer to $z^* > 7.25$, i.e., in the region of the backward current above the interface layer. However, it should be borne in mind that problems in the determination of R_f due to countergradient effects are also present in B/ε and, similarly to what was observed in Fig. 7b, SC shows systematically lower B/ε than RC.

4. CONCLUSIONS

The aim of the present work was to further our knowledge on the effects of bottom roughness on turbulent mixing within the sheared density interface forming at the top of a gravity current. This research was motivated by the still partial knowledge of the applicability of turbulence closure laws commonly adopted in numerical simulations of stably stratified flows of relevance to both geophysical and engineering problems. Two cases were explored: smooth and rough bottom, the latter referring to a planar area index belonging to the range of wake-interference regime.

Our laboratory data show a dependence on the surface roughness of the density interface thickness, which is lower in the case of a rough bottom, as well as of the main parameters involved in the turbulence kinetic energy equation, namely, buoyancy, B, production, P, and its dissipation rate, ε. A substantial dependence on the bottom characteristics was also observed for the turbulent diffusivity of mass and momentum. Conversely, their ratio, i.e., the turbulent Schmidt number, remains essentially unchanged going from the smooth to the rough case. Furthermore, a balance between P, B, and ε was observed across the density interface, particularly for the smooth case, thus verifying the applicability of established buoyancy laws reported in the literature.[40]

Some of the results are consistent with existing field data and numerical simulations, e.g., mixing coefficient B/ε agrees reasonably well with field campaign data[55] irrespective of the surface characteristics.

Further work should focus on expanding the range of surface roughness elements, both two- and three-dimensional, also including vegetated canopies. Additional analysis should also focus on how the relationship between dense current thickness and obstacle height can influence the characteristics of the interface.

ACKNOWLEDGEMENTS

This work has been funded by Sapienza University of Rome, Grant number RM1221816231B1A4.

DATA AVAILABILITY

The data that support the findings of this study are available from the corresponding author upon reasonable request.

AUTHOR DECLARATIONS

CONFLICT OF INTEREST

The authors have no conflicts to disclose.

AUTHOR CONTRIBUTIONS

Conceptualization: Giulia Ravizza Garibaldi (equal), Annalisa Di Bernardino (equal), Paolo Monti (equal)

Data curation: Giulia Ravizza Garibaldi (equal), Annalisa Di Bernardino (equal), Paolo Monti (equal)

Formal analysis: Giulia Ravizza Garibaldi (equal), Annalisa Di Bernardino (equal), Agnese Pini (equal), Giovanni Leuzzi (equal), Giorgio Querzoli (equal), Paolo Monti (equal)

Funding acquisition: Paolo Monti

Investigation: Giulia Ravizza Garibaldi (equal), Annalisa Di Bernardino (equal), Agnese Pini (equal), Giovanni Leuzzi (equal), Giorgio Querzoli (equal), Paolo Monti (equal)

Methodology: Giulia Ravizza Garibaldi (equal), Annalisa Di Bernardino (equal), Paolo Monti (equal), Giorgio Querzoli (equal)

Project administration: Paolo Monti

Software: Giulia Ravizza Garibaldi (equal), Annalisa Di Bernardino (equal), Giorgio Querzoli (equal), Paolo Monti (equal)

Supervision: Annalisa Di Bernardino (equal), Paolo Monti (equal)

Writing – original draft: Giulia Ravizza Garibaldi (equal), Annalisa Di Bernardino (equal), Paolo Monti (equal)

Writing – review & editing: Giulia Ravizza Garibaldi (equal), Annalisa Di Bernardino (equal), Agnese Pini (equal), Giovanni Leuzzi (equal), Giorgio Querzoli (equal), Paolo Monti (equal)

REFERENCES

[1] H. J. S. Fernando, "Turbulent Mixing in Stratified Fluids," Annu. Rev. Fluid Mech. 23, 455–493 (1991).
[2] J. E. Simpson, "Gravity currents in the environment and the laboratory," Cambridge University Press, Cambridge (1997).
[3] W. D. Smyth and J. N. Moum, "Ocean mixing by Kelvin-Helmholtz instability," Oceanography 25, 140-149 (2012).
[4] I. D. Lozovatsky and H. J. S. Fernando, "Mixing efficiency in natural flows," Phil. Trans. R. Soc. A.3712012021320120213 (2013).
[5] P. S. Yeates, A. Gómez-Giraldo, and J. Imberger, "Observed relationships between microstructure patches and the gradient Richardson number in a thermally stratified lake," Environ. Fluid Mech. 13, 205–226 (2013).
[6] J. W. Miles, "On the stability of heterogeneous shear flows," J. Fluid Mech. 10, 496-508 (1961).
[7] L. N. Howard, "Note on a paper of John W. Miles," J. Fluid Mech. 10, 509-512 (1961).

[8] C. P. Caulfield, "Layering, mixing, and turbulence in stratified flows," Annu. Rev. Fluid Mech. 53, 113-145 (2001).
[9] W. R. Peltier and C. P. Caulfield, "Mixing efficiency in stratified shear flows," Annu. Rev. Fluid Mech. 35, 135-167 (2003).
[10] P. G. Baines, "Topographic effects in stratified flows," Cambridge University Press. New York (1997).
[11] Q. Ye, F. Avallone, D. Ragni, and D. Casalino, "Boundary layer transition induced by roughness arrays over NACA 0012 airfoil," Exp. Therm. Fluid Sci. 168, 111505 (2025).
[12] H. J. S. Fernando, "Fluid Dynamics of Urban Atmospheres in Complex Terrain," Annu. Rev. Fluid Mech. 42, 365–89 (2010).
[13] K. B. Winters, P. N. Lombard, J. J. Riley, and E. A. D'Asaro, "Available potential energy and mixing in density-stratified flows", J. Fluid Mech. 289, 115-128 (1995).
[14] C. Staquet, "Mixing in stably stratified shear layer: two- and three-dimensional numerical experiments," Fluid Dyn. Res. 27, 367 (2000).
[15] A. Mashayek and W. R. Peltier, "The 'zoo' of secondary instabilities precursory to stratified shear flow transition. Part 1: Shear aligned convective instabilities," J. Fluid Mech. 725, 216-261 (2011).
[16] V. Armenio and S. Sarkar, "An investigation of stably stratified turbulent channel flow using large-eddy simulation," J. Fluid Mech. 459, 1–42 (2002).
[17] S. K. Venayagamoorthy and J. R. Koseff, "On the flux Richardson number in stably stratified turbulence," J. Fluid Mech. 798: R1 (2016).
[18] X. Huo, Q. Xu, H. Gao, L. Lang, and Y. Zhang, "Characterizing turbulent mixing and entrainment in gravity currents sustained by constant inflow," Phys. Fluids 37(10), 106603 (2025).
[19] P. Monti, H. J. S. Fernando, M. Princevac, W. C. Chan, T. A. Kowalewski, and E. R. Pardyjak, "Observations of flow and turbulence in the nocturnal boundary layer over a slope," J. Atmos. Sci. 59, 2513–2534 (2002).
[20] A. A. Grachev, L. S. Leo, S. Di Sabatino, H. J. S. Fernando, E. R. Pardyjak, and C. W. Fairall, "Structure of Turbulence in Katabatic Flows Below and Above the Wind-Speed Maximum," Boundary-Layer Meteorol. 159, 469-494 (2016).
[21] C. Charrondière, C. Brun, J. E. Sicart, J. M. Cohard, R. Biron, and S. Blein, "Buoyancy effects in the turbulence kinetic energy budget and Reynolds stress budget for a katabatic jet over a steep alpine slope," Boundary-Layer Meteorol. 177, 97–122 (2020).
[22] M. R. Maggi, M. E. Negretti, E. J. Hopfinger, and C. Adduce, "Turbulence characteristics and mixing properties of gravity currents over complex topography," Phys. Fluids 35, 016607 (2023).
[23] M. R. Maggi, G. Di Lollo, and C. Adduce, "Dynamics and mixing of gravity currents over an array of cylindrical obstacles," Phys. Fluids 37, 076629 (2025).
[24] P. F. Linden and J. E. Simpson, "Gravity-driven flows in a turbulent fluid," J. Fluid Mech. 172, 481-497 (1986).
[25] H. I. Nogueira, C. Adduce, E. Alves, and M. J. Franca, "Analysis of lock-exchange gravity currents over smooth and rough beds," J. Hydraul. Res. 51, 417–431 (2013).
[26] L. Ottolenghi, C. Adduce, R. Inghilesi, V. Armenio, and F. Roman, "Entrainment and mixing in unsteady gravity currents," J. Hydraul. Res. 54, 541-557 (2016).
[27] C. Cenedese, T. Nokes, and J. Hyatt, "Lock-exchange gravity currents over rough bottoms," Environ. Fluid Mech. 18, 59–73 (2018).
[28] S. Longo, M. Ungarish, V. Di Federico, L. Chiapponi, D. Petrolo, "Gravity currents produced by lock-release: Theory and experiments concerning the effect of a free top in non-Boussinesq systems," Adv. Water Resour. 121, Pages 456-471 (2018).
[29] C. D. Troy and J. R. Koseff, "The generation and quantitative visualization of breaking internal waves," Exp. Fluids. 38, 549–562 (2005).
[30] A. Cenedese, Z. Del Prete, M. Miozzi, and G. Querzoli, "Laboratory investigation of the flow in the left ventricle of a human heart with prosthetic, tilting-disk valves," Exp. Fluids 39, 322–335 (2005).
[31] C. S. B. Grimmond and T. R. Oke, "Aerodynamic properties of urban areas derived from analysis of urban surface form," J. Appl. Meteorol. 38, 1261-1292 (1999).
[32] H. J. S. Fernando, D. Zajic, S. Di Sabatino, R. Dimitrova, B. Hedquist, and A. Dallman, "Flow, turbulence, and pollutant dispersion in urban atmospheres," Phys. Fluids 22, 051301 (2010).

[33] D. Xu and J. Chen, "Experimental study of stratified jet by simultaneous measurements of velocity and density fields," Exp Fluids 53:145–162 (2012).
[34] R. Buccolieri, H. Wigö, M. Sandberg, and S. Di Sabatino, "Direct measurements of the drag force over aligned arrays of cubes exposed to boundary-layer flows," Environ Fluid Mech. 17, 373–394 (2017).
[35] M. E. Negretti, D. Z. Zhu, G. H. Jirka, "The effect of bottom roughness in two-layer flows down a slope," Dyn. Atmos. Oceans 45, 46-68 (2008).
[36] G. Constantinescu, "LES of lock-exchange compositional gravity currents: a brief review of some recent results," Environ. Fluid Mech. 14, 295–317 (2014).
[37] G. I. Taylor, "Statistical theory of turbulence," Proc. R. Soc. Lond. A 151, 421 (1935).
[38] J. Hinze, "Turbulence" McGraw-Hill, New York (1975).
[39] H. Tennekes and J. L. Lumley, "A First Course in Turbulence," MIT Press (1972).
[40] T. R. Osborne, "Estimates of the local rate of vertical diffusion from dissipation measurements," J. Phys. Oceanogr. 10, 83–89 (1980).
[41] R. Longo, M. Fürst, A. Bellemans, M. Ferraroi, M. Derudi, and A. Parente, "A CFD dispersion study based on a variable Schmidt formulation for flows around different configurations of ground-mounted buildings," Build. Environ. 154, 336-347 (2019).
[42] C. Gorlé, J. van Beeck, and P. Rambaud, "Dispersion in the wake of a rectangular building: validation of two Reynolds-averaged Navier-Stokes modelling approaches," Boundary-Layer Meteorol. 137, 115-133 (2010).
[43] A. Di Bernardino, P. Monti, G. Leuzzi, and G. Querzoli, "Turbulent Schmidt Number Measurements Over Three-Dimensional Cubic Arrays," Boundary-Layer Meteorol. 174, 231-250 (2020).
[44] C. Vidali, M. Marro, L. Gostiaux. et al., "Wind-Tunnel Experiment of Heavy Gas and Passive Scalar Emission in a Turbulent Boundary Layer," Boundary-Layer Meteorol. 191, 18 (2025).
[45] Y. Tominaga and T. Stathopoulos, "CFD modeling of pollution dispersion in building array: evaluation of turbulent scalar flux modeling in RANS model using LES results," J. Wind Eng. Ind. Aerodyn 99, 340–348 (2012).
[46] M. E. Barry, G. N. Ivey, K. B. Winters, and J. Imberger, "Measurements of diapycnal diffusivities in stratified fluids," J. Fluid Mech. 442, 267-291 (2001).
[47] R. B. Stull, "An introduction to boundary layer meteorology," Kluwer, Dordrecht (1988).
[48] C. Charrondière, C. Brun, E. J Hopfinger, J. -M. Cohard, and J. -E. Sicart, "Mean flow structure of katabatic winds and turbulent mixing properties," J. Fluid Mech. 941, 941:A11. (2022)
[49] L. Marth and D. Vickers, "Formulation of turbulent fluxes in the stable boundary layer," J. Atmos. Sci. 60, 2538_2003 (2003).
[50] E. J. Strang and H. J. S. Fernando, "Entrainment and mixing in stratified shear flows," J. Fluid Mech. 428, 349-386 (2001).
[51] K. B. Winters and E. A. D'asaro, "Diascalar flux and the rate of fluid mixing," J. Fluid Mech. 317, 179 (1996).
[52] G. N. Ivey and J. Imberger, "On the nature of turbulence in a stratified fluid. Part I: the energetics of mixing," J. Phys. Oceanogr. 21, 650–658 (1993).
[53] L. H. Shih, J. R., Koseff, G. N. Ivey, and J. H. Ferziger, "Parameterization of turbulent fluxes and scales using homogeneous sheared stably stratified turbulence simulations," J. Fluid Mech. 525, 193–214 (2005).
[54] G. N. Ivey, "Turbulence in the Environment. Handbook of Environmental Fluid Dynamics," Vol One. Fernando H. J. S. ed., Taylor and Francis (2013).
[55] P. Conry, E. Kit, and H. J. S. Fernando, "Measurements of mixing parameters in atmospheric stably stratified parallel shear flow," Environ. Fluid Mech. 20, 1177–1197 (2020).
[56] H. J. S. Fernando, E. R. Pardyjak, S. Di Sabatino, et al., "The MATERHORN: unraveling the intricacies of mountain weather," Bull. Am. Meteorol. Soc. 96, 1945–1968 (2015).